Relationship between mechanical amorphization and boron integration during processing of FeNbB alloys

J.J. Ipus[1], J.S. Blázquez[1], C.F. Conde[1], J.M. Borrego[1], V. Franco[1], S. Lozano-Perez[2], A. Conde[1]

[1] Departamento de Física de la Materia Condensada, ICMSE-CSIC, Universidad de Sevilla, P.O. Box 1065, 41080, Sevilla, Spain.

[2] Department of Materials, University of Oxford, Parks Road, Oxford OX1 3PH, UK.

Abstract

$Fe_{75}Nb_{10}B_{15}$ alloys were prepared by mechanical alloying using different boron powders (crystalline B, commercial amorphous B, optimized amorphous B and intermetallic FeB) in the initial mixture, in order to study the boron incorporation into the Fe matrix and its influence on the amorphization of the alloys. Another composition with the same Fe/Nb ratio but whithout boron was prepared in order to differentiate between the influence of B and Nb in the evolution of microstucture and magnetic properties. Amorphization of samples was followed by X-ray diffraction and Mössbauer spectroscopy, concluding that only B-containing alloys develop an amorphous phase, while for the B-free alloy a supersaturated solid solution was observed as the final microstructure. Nb is rapidly incorporated into the matrix whereas remaining B inclusions are found at the end of the explored milling range for all B-containing samples. The amount of dissolved boron into the amorphous matrix was estimated from magnetic measurements, being the alloy prepared using FeB powder the one that most effectively dissolves this element.

Keywords: C. Mechanical alloying and milling; B. Magnetic properties;

1.   Introduction

Fe-based amorphous and nanocrystalline alloys have been amply studied due to their improved magnetic properties, which can be strongly enhanced with respect to those exhibited by conventional microstructures [1]. Nanocrystalline Fe-M-B type alloys, so called Nanoperm where M is an early transition metal, have been attractive for their excellent soft magnetic properties and are used as ultrasoft magnets in several commercial applications [1,2]. These good soft magnetic properties depend on the microstructure of the material [3,4].

These systems are generally obtained by rapid quenching techniques and followed by a subsequent optimal annealing treatment. The former step assures a good homogenization of the precursor amorphous alloy because the starting point is a liquid. Another way to produce these compositions is using mechanical alloying, which has become a very versatile technique to directly produce metastable microstructures (nanocrystalline, supersaturated solid solutions, amorphous, etc) [5] from elemental powder constituents and its use in the production of soft magnetic alloys is increasing [6]. During the milling process, the material is continuously submitted to fracture and cold welding phenomena, as well as intensive plastic deformation, which refine the powder morphology and define the microstructure and properties of these materials. Several theoretical and experimental works have shown that some rules that apply in the construction of phase diagrams for macroscopic alloy systems fail for small particles [7,8,9,10], (e.g. melting temperature decreases, liquid-solid line moves towards the solid composition band and solubility range increases with respect to bulk materials).

Boron is an element generally used in amorphous and nanocrystalline compositions as a glass former element and to extend the thermal stability of these metastable materials. The former role is especially important when the amorphous alloy is produced by rapid quenching

(which restricts compositions close to eutectics) and the enhancement of thermal stability is valuable regardless the production technique. However, the boron distribution in the alloy depends on the processing and boron inclusions in Fe-based alloys are found even after long milling times in mechanically alloyed powders [11,12,13].

Previously, we have found that when amorphous boron is used instead of crystalline one in the initial mixture to be milled, the formation of the amorphous phase is accelerated, developing a larger fraction for the same milling time [14]. In this work, a $Fe_{75}Nb_{10}B_{15}$ composition is prepared by mechanical alloying and, in order to study the enhancement of boron dissolution into the nanocrystalline/amorphous matrix, different boron powders were used. A B-free composition keeping the same Fe/Nb ratio, 75:10, was prepared for comparison.

2. Experimental

2.1 *Microstructure of initial boron powder*

For $Fe_{75}Nb_{10}B_{15}$ sample preparation, the 15 at.% B of the starting mixtures was supplied in four different initial microstructures. Figure 1(a-c) shows the X-ray diffraction (XRD) patterns of their microstructures. Two of them were commercial pure boron powders: crystalline single phase β-B ($R\overline{3}m$ space group) with lattice parameters $a =b =10.925$ Å and $c =23.814$ Å (Fig.1a); an commercial amorphous boron (Fig.1b upper curve) composed of ~35% of β-B, ~15% of $(N_3)(NB_9H_{11})$ and only ~50% of amorphous phase. In order to increase the amorphous phase fraction of this boron powder, ball milling of commercial amorphous powder was performed (Fig.1b). A mass of 30 g of commercial amorphous boron powder was milled in a planetary ball mill Fritsch Pulverisette 4 Vario, with steel balls and hardened steel vials, up to 50 h in Ar atmosphere. In order to minimize Cr-contamination of the milled powder, low Cr-content balls

were used. Microanalysis of all the studied samples shows no detectable signal of this element. The ball to powder ratio was 10:1 and the rotational speed of the main disc was 350 rpm and that of the vials was 700 rpm in opposite direction. XRD patterns of figure 1b show that, as milling progresses, crystalline diffraction maxima disappear and, finally, only amorphous halo is observed for milling times larger than 10 h. Therefore, after milling, the amorphous fraction increases from ~50 % for commercial to ~100 % for as-milled boron powders. However, (110) diffraction line of α-Fe is also found due to contamination from milling media. As EDX detection of small changes in Fe concentration of Fe-rich FeB alloys is not feasible, microanalysis experiments were performed on mechanically alloyed Fe-free compositions prepared with this optimized amorphous boron. From this analysis, the estimated composition of the optimized amorphous boron is $B_{95}Fe_5$ [15]. Further milling, t >50 h, leads to recrystallization of the boron powder. Figure 1c shows the XRD pattern of the commercial intermetallic FeB (1:1 stoichiometry) powder used, showing a single phase. However, scanning electron microscopy (SEM) image in backscattering (BS) mode and energy dispersive X-ray analysis on this raw FeB powder reveal the existence of almost pure boron regions (see black regions in BS image of figure 1d).

2.2   Sample preparation and experimental techniques

Alloys with nominal composition $Fe_{75}Nb_{10}B_{15}$ were prepared using powders of: crystalline boron ≥99 % purity (Chempur: Basis Art. Nr. 009054), denoted as c-B alloy; commercial amorphous boron 95-97% purity (Chempur: Basis Art. Nr. 009049), a-B alloy; optimized amorphous boron, a2-B alloy; or intermetallic FeB 99 % purity (Chempur: Basis Art. Nr. 900927), FeB alloy, along with elemental Fe and Nb powders ≥99 % purity. For a2-B alloy, due to the previous milling process for obtaining the optimized amorphous boron, the samples

are submitted to a longer overall time of milling. A fifth alloy without boron (n-B) with the same

Fe/Nb ratio was also prepared. Mixtures of 30 g of these powders were used as starting materials

in the planetary mill described above with the same milling parameters. After selected milling

times, some powder was taken out from the vials to characterize its microstructure and magnetic

properties as a function of milling time. Opening and closing of vials were done under Ar

atmosphere in a Saffron Omega glove box to avoid oxygen and humidity contamination.

Present phases and microstructure evolution were studied by XRD, using Cu Kα radiation

in a Bruker D8I diffractometer. Local environment of Fe atoms was analyzed by Mössbauer

spectrometry (MS), at room temperature in a transmission geometry using a ^{57}Co(Rh) source.

The values of the hyperfine parameters were obtained by fitting with NORMOS program [16]

and the isomer shift (IS) was quoted relative to that of an α-Fe foil at room temperature. Thermal

stability of the samples was studied by differential scanning calorimetry (DSC) using a Perkin-

Elmer DSC7 under Ar flow. Morphology of powders was studied by scanning electron

microscopy (SEM) using secondary (SE) and backscattered electrons (BSE) images in a Jeol

JSM-6460 LV and equipped with an energy dispersive X-ray (EDX) analyzer (Incax-sight of

Oxford Instruments).

Local microstructure was studied by transmission electron microscopy (TEM) using a

Jeol JEM3000F microscope operated at 297 kV. Scanning transmission electron microscopy

(STEM) mode was used to obtain high-angle annular dark field (HAADF) images and selected

area electron diffraction (SAED) patterns were used to identify the present phases. Electron

energy loss spectroscopy (EELS) was used for boron detection with a Gatan image filter (GIF)

2002, which provided an energy resolution of ~1 eV. Sample preparation was performed by

focused ion beam (FIB), using a FEI 200 and a Zeiss NVision 40, extracting a TEM transparent slide from an individual powder particle following the lift out procedure [17].

Isothermal magnetization curves were measured using a Lakeshore 7407 vibrating sample magnetometer (VSM) with a maximum applied field of H=1.5 T, field steps of 250 Oe, in the temperature range of 77-390 K with increments of 10 K. Spontaneous specific magnetization, σ_0, was obtained from the extrapolation of high field magnetization curves, $\sigma(H)$, to zero field. Curie temperature, T_C, was calculated as the inflexion point of σ_0 (T) curves.

3.   Results

3.1   X-ray diffraction

XRD patterns show that, for times $t \leq 4$ h, diffraction peaks of both phases, bcc-Fe and bcc-Nb, are clearly distinguishable. As milling progress, for $t \geq 4$ h, peaks corresponding to bcc-Nb phase disappear as Nb atoms dissolve in the α-Fe and crystal boundaries. Figure 2(a-c) shows the XRD patterns of the different samples after selected times and figure 3 shows the evolution of Nb phase fraction with milling time, calculated as the area ratio between (110) maximum of bcc-Nb and the sum of (110) maxima of bcc-Fe and bcc-Nb. Their different atomic scattering factors were taken into account but interdiffusion between Fe and Nb was neglected. It can be observed that all samples present a Nb phase fraction around the nominal one at 0.5 h and, for longer milling times, the rate of reduction is almost similar and independent of the presence of boron in the sample, ~-4 at.%/h. For a-B and a2-B samples the Nb fraction is zero after 4 h milling, while bcc-Nb fraction is not detected after 3.5 h milling for the other alloys.

XRD patterns show a similar behavior for all samples up to 4 h milling, where a shift to lower angles of (110) bcc-Fe peak (due to the incorporation of Nb atoms into the Fe lattice) and a

broadening of this peak are observed. These features are ascribed to the formation of a bcc-Fe(Nb) supersaturated solid solution as well as to the increase of microstrains and crystal size refinement. For longer milling times, $t \geq 6$ h, a continuous broadening of the (110) bcc-Fe(Nb) peak is observed only for B-containing samples, which is related to the formation of an amorphous phase. In the case of B-free sample, the supersaturated solid solution was the final microstructure and the broadening and the angular position of (110) line of bcc-Fe(Nb) phase are almost stabilized after 4 h milling.

Analysis of the XRD patterns was performed by a deconvolution of the (110) bcc-Fe diffraction peak and the amorphous halo using Lorentzian and Gaussian profiles to represent the crystalline and amorphous contributions, respectively. Crystalline fraction, X_C, has been estimated from the ratio between the area of the Lorentzian contribution and the total area of diffraction peak (Lorentzian plus Gaussian) and its evolution as a function of milling time is shown in figure 4 for B-containing samples. It can be seen that X_C continuously decreases with milling due to a progressive amorphization, but X_C remains almost constant for $t \geq 30$ h.

3.2 Mössbauer spectroscopy

Local Fe neighborhoods as a function of milling time have been studied by MS and figure 5 shows MS spectra and hyperfine field distribution for samples after 40 h milling. After 0.5 h all spectra can be described using a single bcc-Fe environment, corresponding to a sextet with hyperfine field, $HF = 33$ T. For longer milling times, the formation of new Fe environments with $HF < 33$ T are observed. These new neighborhoods could be related to Fe in a bcc environment but in the presence of impurities and/or Fe atoms located in the interphase region of the nanocrystals [18]. Other kinds of environments with very low hyperfine fields, $HF \leq 5$ T, are also observed in the spectra for all samples, regardless their boron content. These low HF

contributions are associated with Fe atoms surrounded by a large number of Nb atoms as neighbors. Although the evolution of these low *HF* contributions is similar for all the studied alloys for $t \leq 4$ h, this contribution decreases for longer milling times for B-free sample, reaching a constant value after 10 h. In the case of B-containing samples, this contribution (*HF* ≤ 5 T) continuously increases with milling time becoming the main contribution at the end of milling. Figure 6 shows the evolution of the fraction of Fe atoms in Nb rich environments, i.e. those with *HF* ≤ 5 T ($C_{Fe}^{(HF \leq 5T)}$). The fitting of this kind of complex spectra implies some ambiguity and these low field contributions can represent pure paramagnetic sites as a singlet would do.

3.3 Electron microscopy

Size of powder particles was measured by SEM showing, initially, values above hundred microns, which rapidly decrease reaching a minimum of some tens of microns after 4 h. Further milling leads to the formation of agglomerates. Figure 7(a-d) shows BSE images for samples after 40 h milling, in which it is possible to observe B inclusions as dark spots. However, other microstructural features such as cracks, topography of powders, etc, giving rise to dark regions, complicate a quantitative analysis. Therefore, in the present study, TEM studies using HAADF technique have been used in order to determine the dependence of the number density of B inclusions on starting boron microstructure. In figure 7(f-h) HAADF images also show that boron inclusions are present in all samples, even in that prepared using intermetallic FeB powder, although the number density of boron inclusions clearly decreases for this alloy with respect to the other ones. A TEM image for c-B alloy (Fig. 7e), taken from [11] is also shown for comparison (note the different magnification). This implies better boron dissolution into the matrix when FeB powder is used than when the starting mixture is prepared with pure boron. In fact, the remaining boron inclusions observed for FeB sample could be ascribed to the pure

boron regions detected in the used intermetallic powder (see SEM image in Fig 1d). EDX analysis results of all the B-containing alloys after 40 h milling are collected in table 1. Nominal starting values are also shown. No significant difference are observed in Fe/(Fe+Nb) ratio (~0.2 %). Cr contamination is shown to be less than 1 at. % in any case.

Local microstructure has been previously studied by TEM for c-B [11] and a-B [14] samples. Similar results were found for alloys subject of the present study. After 40 h milling a microstructure composed by an amorphous matrix with dispersed bcc-Fe(NbB) nanocrystals (~5 nm) and crystalline boron inclusions (~30 nm) is observed, as is presented in the bright field image for a2-B sample after 40 h milling shown in figure 8.

3.4   *Thermal stability*

DSC scans of samples after 40 h milling are shown in figure 9 along with the corresponding scan for a $Fe_{75}Nb_{10}B_{15}$ amorphous ribbon obtained by melt spinning, for comparison. A broad exothermic process below 800 K is observed for all the powder samples. For powder alloys, this phenomenon is observed for temperatures as low as 400 K. Taking into account that, in the present case, no phase changes have been detected, the observed effect sould be associated to some relaxation phenomena (stress and free volume release) or phase stabilization (compositional adjustment of the crystalline phase). Crystallization process takes place in two steps at temperatures ~850 K and ~950 K, as it is also observed for melt spun sample. Table 2 shows values of crystallization peak temperature at 40 K/min, T_p, and activation energy, E_A, obtained from Kissinger method [19] for the main crystallization process. The activation energy decreases as c-B >a-B >a2-B >FeB samples, approaching the value of the ribbon sample.

3.5   *Magnetic properties*

Figure 10 shows room temperature spontaneous specific magnetization, σ_0, as a function of milling time for all studied samples. Two different behaviors can be observed: for the B-free sample an initial reduction in σ_0 is detected up to 4 h, followed by an increase reaching a stable value of ~145 emu/g after $t \geq 10$ h, which should be ascribed to the formation of a bcc-Fe(Nb) supersaturated solid solution. For B-containing samples, σ_0 continuously decreases as milling progresses due to the formation of the paramagnetic amorphous phase, in agreement with the above described evolution of low HF contribution. Although no samples reach zero σ_0 value due to the presence of remaining bcc-Fe(NbB) crystals, the faster reduction of σ_0 for the FeB sample is related to a faster development of the amorphous phase when compared to the other B-containing samples, in agreement with the microstructural results.

Figure 11 shows the milling time dependence of the Curie temperature, T_C, of the developed amorphous phase for all the boron containing alloys. It can be seen that T_C continuously increases for all samples, which can be ascribed to a progressive boron enrichment of the amorphous matrix due to dissolution of this element after a slow refinement of boron inclusions. In fact, a small increase of ~3 at.% B in the amorphous phase could explain an increase of ~40 K in its Curie temperature [20].

4.   Discussion

4.1   Microstructure

Concerning the decrease in X_C shown in figure 4, although X_C decreases faster for a-B, a2-B and FeB samples than for the c-B one, the reduction rate for FeB sample is the highest among the studied alloys and X_C reaches very low values (0.05 for $t \geq 20$ h), within the estimated error of our analysis. Taking into account that boron is necessary to develop the amorphous

phase, it can be inferred that boron content of the matrix increases in the order c-B <a-B ≈a2-B< FeB. Therefore, for the FeB alloy the rate of boron dissolution into the matrix is the highest among the studied samples.

Lattice parameter, a, crystal size and microstrains were calculated using TOPAS software and figure 12 shows the evolution of these parameters as a function of milling time. To simulate the amorphous contribution in these fits, first a bcc contribution with large lattice parameter, very small crystal size and large microstrains was used to fit the pattern with lowest X_C. Then after fixing all parameters except for its peak position and area, this contribution was used to fit the other patterns. As X_C decreases, errors in determining the position corresponding to the bcc phase increases. Therefore, lattice parameter, crystal size and microstrains data are not shown when a very low fraction (X_C <0.1), was obtained. A refinement of crystal size and an increase of microstrains up to 4 h milling are observed with constant values for longer milling times. It is worth mentioning that crystal size is larger for n-B sample than for any B-containing alloy, which could be ascribed to the presence of boron inclusions. These inclusions should play the role of extra milling media, helping to reduce the crystal size.

Lattice parameter initially increases as the supersaturated solid solution is formed. Maximum value of a is reached after 6 h milling for c-B sample and after 10 h milling for the other alloys, being the value for n-B alloy the largest one, a = 2.917 ±0.002 Å, while maximum values for the other alloys are: a= 2.902 ±0.008 Å, 2.899 ±0.007 Å, 2.899 ±0.007 Å and 2.883 ±0.003 Å for c-B, a-B, a2-B and FeB samples, respectively. Further milling keeps a values almost constant for B-containing samples. However, for the n-B alloy a decrease is clearly observed, which could be related to a Fe enrichment due to contamination from milling media.

The Nb content of the bcc-Fe(Nb) solid solution for n-B sample can been estimated from a values using Vegard law, as 11.6 ±0.1 at.%, in agreement with the corresponding value of the nominal composition. The lower values of a for boron containing samples could be explained by the incorporation of B atoms into the bcc-Fe(Nb) lattice [21], pointing to a larger boron dissolution for FeB alloy than for a-B or a2-B alloys and less dissolution for c-B alloy.

4.2   Local environments

Concerning the evolution of the fraction of Fe atoms in Nb rich environments shown in Fig. 6, for $t \leq 4$ h, an increase in $C_{Fe}^{(HF \leq 5T)}$ is common for all samples, regardless the type of boron used. Thus, this fraction should be related with both the high introduction of Nb atoms into the bcc-Fe lattice and the incorporation of Fe atoms into the Nb lattice, excluding any role of B in this evolution. In fact, when the milling starts, there are no Nb atoms in the bcc-Fe phase or viceversa and all Fe atoms should be in pure bcc-Fe sites (33 T). For relative short milling times, $t = 4$ h, ductile Nb crystals appear elongated increasing their surface, as shown in EDX maps of ref. [11]. Therefore, there is an enhanced fraction of Fe atoms facing the surface of these Nb crystals, whereas a large population of Fe atoms shows no significant Nb in their neighborhoods ($HF = 33$ T). For milling times $t > 4$ h, $C_{Fe}^{(HF \leq 5T)}$ decreases for n-B sample reaching a stable minimum value for 10 h milling. However, a continuous increase of $C_{Fe}^{(HF \leq 5T)}$ is observed for B-containing samples, with a rate of increase following the trend: FeB >a2-B >a-B >c-B. While the reduction of $C_{Fe}^{(HF \leq 5T)}$ for n-B alloy can be explained by an homogenization of Nb atoms in Fe matrix, the increase of $C_{Fe}^{(HF \leq 5T)}$ for boron containing samples is in agreement with the observed behavior of X_C, from XRD results. Therefore, the evolution of $C_{Fe}^{(HF \leq 5T)}$ for $t > 4$ h can be related to the development of a paramagnetic amorphous phase. However, a reduction in $C_{Fe}^{(HF \leq 5T)}$ for FeB sample is observed for $t \geq 30$ h, which is related to the appearance of contribution with HF

between 5 and 20 T, also observed for melt spun ribbons of the same composition and ascribed to an enlargement of the Fe-Fe distance in the matrix [22].

For a binary bcc Fe-Nb alloy we can obtain the probability of getting different Fe environments from the fitting of the spectra using binomial distributions considering the near neighborhoods (NN) and next near neighborhoods (NNN). We can estimate the concentration of Nb atoms in the bcc Fe(Nb) phase, *C(Nb)*, from the ratio between contributions with 33 T and ~30 T corresponding to Fe atoms with 0 and 1 Nb in their environments, respectively [23]. The probability to find a Fe atom with *n* Nb as NN or NNN is expressed as:

$$P(n) = \frac{14!}{(14-n)!n!} C(Fe)^{14-n} C(Nb)^n \tag{1}$$

where *C(i)* refers to Fe and Nb concentrations in the probe configuration formed by 14 atoms surrounding a central Fe atom. Calculating the ratio between probabilities *P(1)* and *P(0)* we obtain:

$$\frac{P(1)}{P(0)} = \frac{14\left[1-C(Nb)\right]^{13} C(Nb)}{\left[1-C(Nb)\right]^{14}} \tag{2}$$

and the Nb concentration in the binary Fe-Nb system could be obtained as:

$$C(Nb)^* = \frac{14}{15}\left[\frac{\dfrac{P(1)}{P(0)}}{14+\dfrac{P(1)}{P(0)}}\right] \tag{3}$$

where *C(Nb)*=(14/15)C(Nb)* is the Nb concentration in the alloy, unlike *C(Nb)*, which corresponds to the Nb concentration in the set of 14 atoms surrounding a 15th Fe atom.

Figure 13 shows the obtained values of Nb concentration as a function of milling time for all studied alloys. It can be seen that Nb content in bcc-Fe crystals rapidly increases for all

studied alloys with a similar rate for times $t \leq 6$ h. As errors in this analysis increase as X_C increases, data for B-containing alloys are shown only up to $t=6$ h. For n-B alloy *C(Nb)* gets a maximum value after 10 h milling in agreement with the evolution of *a* described before. Further decrease in *C(Nb)* for this alloy is ascribed to Fe contamination from milling media for long milling times, which is also in agreement with lattice parameter results.

The values obtained from this analysis refer to core sites in bcc-Fe, as Fe atoms in interphase regions should exhibit a reduction in their corresponding *HF* values. In fact, Nb content in core sites increases up to 90% of the nominal value, which can be understood due to a Nb enrichment in crystalline boundaries.

4.3 *Magnetic properties*

From magnetization measurements of n-B sample we can also follow the incorporation of Nb into the nanocrystalline bcc-Fe(Nb) matrix. Taking into account values of theoretical magnetic moment for binary bcc-$Fe_{100-X}Nb_X$ crystals [24], we have first calculated the theoretical specific magnetization, σ_0, values as a function of X in the range from 0 to 20 at.%. Then, we have fitted those values to a straight line, as shown in figure 14. Using this linear relationship and our experimental σ_0 data we have estimated the Nb content for the n-B sample. A continuous increase in Nb up to 4 h milling can be seen when magnetization reaches its minimum value. For times between 10 and 40 h milling an almost constant value of Nb content is found, ~13 at.%, which agrees with the value from the nominal composition, in agreement with above results. Therefore, we can consider that for $t \geq 10$ h the B-free sample has all Nb atoms in the crystalline Fe(Nb) matrix and a constant magnetization. This result has been extrapolated to the case of B-containing samples, and thus we will assume that Nb is completely integrated in the remaining crystalline phase as well as in the developed amorphous phase.

As Nb content could be considered constant in the amorphous matrix for $t \geq 10$ h milling, we can estimate the amount of dissolved boron into the matrix from the T_C values after this time. In figure 15, Curie temperature data for amorphous $Fe_{100-Y}B_Y$ systems are shown [20] and a linear relationship for T_C with Y is obtained. To take into account the effect of 10 at.% Nb in our samples, we have shifted this linear relationship to match the T_C of a melt spun amorphous $Fe_{75}Nb_{10}B_{15}$ ribbon sample, in which both Nb and B are assumed to be completely dissolved into the matrix. Thus, we obtain a relationship for the T_C as a function of boron content for our $(Fe_{75}Nb_{10})_{100-Z}B_Z$ powder samples (Fig 15). For each experimental T_C data and using this straight line we can obtain the boron content; (e.g. for t =40 h B content is: 11, 12, 11 and 14 at.% B for c-B, a-B, a2-B and FeB samples, respectively. The possible of Cr from contamination, a reduction of 25 K/at. % Cr in T_C of the amorphous phase [25], should imply an error below 1 at. % B).

It can be seen that FeB sample is for which the boron is better dissolved in the amorphous matrix, while c-B sample has the lowest dissolved amount. It is worth noticing that, although a2-B alloy has a lower boron content than that a-B sample, the Fe contamination found after processing the commercial amorphous B (used for a-B alloy) to produce the optimized amorphous B (used for a2-B alloy) makes the actual Fe/B ratio in the initial mixture to differ from the nominal value. Figure 16 shows boron content normalized to the initial boron content for each alloy (15 at.% for c-B, a-B and FeB samples and ~14 at.% for a2-B sample) for milling times above 10 h. A progressive increase of boron content in the amorphous matrix with milling time is evidenced and the percentage of B dissolved increases in the order: c-B <a-B ~a2-B <FeB. In fact, the use of FeB powder leads to the best incorporation of boron into the matrix, enhancing its similarity to the melt spun sample.

5.   Conclusions

Mechanical alloying of $Fe_{75}Nb_{10}B_{15}$ composition was performed using different boron powders (crystalline, commercial amorphous, ball milled amorphous and intermetallic FeB) to prepare the initial mixture. Another sample without boron was milled keeping constant the Fe/Nb ratio as a reference to distinguish the effect of boron on the samples.

Microstructural evolution of the samples reveals that boron addition is necessary to develop an amorphous phase via mechanical alloying for the studied Fe/Nb ratio. Moreover, boron containing alloys show smaller crystal size and lattice parameter of the bcc-Fe(Nb) supersaturated solid solution when compared to B-free alloy with the same Fe/Nb ratio.

The rate of amorphization changes with the type of boron used in the initial mixture. This rate (and thus the amount of developed amorphous fraction) increases as c-B <a-B <a2-B <FeB.

The evolution of Fe environments shows the appearance of low *HF* Fe sites by a common enhancement of Nb rich environments at low milling times for all the studied alloys. However, long milling time evolution is related to boron content in the alloy: whereas paramagnetic amorphous phase is developed in B-containing alloys leading to an enhancement of the low *HF* contribution, Nb is homogenized in the Fe matrix and the low *HF* contribution decreases for B-free alloy.

Nb atoms are rapidly incorporated into the Fe matrix and can be assumed as a completed process after 10 h milling under our experimental conditions. However, B is not completely incorporated in the matrix for any of the studied alloys and B inclusions can be observed even after 40 h milling.

Spontaneous specific magnetization decreases as amorphous phase is developed for B-containing alloys, while for B-free alloy a constant value of ~145 emu/g is observed for milling times larger than 10 h, when the solid solution is stabilized. Curie temperature of the amorphous phase is enhanced from ~250 K for c-B alloy to values around room temperature for FeB alloy. The properties shown for FeB sample are the more similar among the studied alloys to those exhibited by a melt spun ribbon of the same composition.

From the Curie temperature evolution, a continuous increase of B content in the amorphous phase with milling was established for all samples, being the largest for FeB alloy. Finally, at the end of milling, the boron content in the matrix for the FeB alloy is ~14 at.% and the undissolved B remains as few inclusions dispersed through the amorphous matrix.

Acknowledgements

Reference

[1]   M.E. McHenry, M.A. Willard, D.E. Laughling, Prog. Mater. Sci. 44 (1999) 291-433.

[2]   A. Makino, T. Hatanai, A. Inoue, T. Matsumoto, Mater. Sci. Eng. A 226-228 (1997) 594-602.

[3]   A. Hernando, M. Vázquez, T. Kulik, C. Prados, Phys. Rev. B 51 (1995) 3581-3586.

[4]   I. Chicinas, N. Jumate, G. Matei, J. Magn. Magn. Mater. 140-144 (1995) 1875-1876.

[5]   C. Suryanarayana, Prog. Mater. Sci. 46 (2001) 1-184.

[6]   J.S. Blázquez, J.J. Ipus, S. Lozano-Perez, A. Conde, JOM 65 (2013) 870-882.

[7]   M. Wautelet, P.J. Dauchot, M. Hecq, Nanotechnology, 11 (2000) 6-9.

[8]   L.H. Liang, D. Liu, Q. Jiang, Nanotechnology 14 (2003) 438-442.

[9]   J. Weissmuller, P Bunzel, G. Wilde, Scripta Mater. 51 (2004) 813-818.

[10]   W.A. Jesser, R.Z. Shneck, W.W. Gile, Phys. Rev. B 69 (2004) 144121:1-13.

[11]   J.J. Ipus, J.S. Blázquez, S. Lozano-Pérez, A. Conde, Philos. Mag. 89 (2009) 1415-1423.

[12]   J.J. Ipus, J.S. Blázquez, A. Conde, M. Krasnowski, T. Kulik, S. Lozano-Pérez, J. Appl. Phys. 107 (2010) 073901:1-6.

[13]   M. Krasnowski, A. Antolak-Dudka, T. Kulik, Intermetallics 19 (2011) 1243-1249.

[14]   J.J. Ipus, J.S. Blázquez, V. Franco, S. Lozano-Pérez, A. Conde, J. All. Compd. 553 (2013) 119-124.

[15]   L.M. Moreno, J.S. Blázquez, J.J. Ipus, A. Conde, J. All. Compd. 585 (2014) 485-490.

[16]   R.A. Brand, J. Lauer, D.M. Herlach, J. Phys. F: Met. Phys. 13 (1983) 675-683.

[17]   S. Lozano-Pérez, Micron 39 (2008) 320-328.

[18]   J.M. Greneche, A. Slawska-Waniewska, J. Mag. Mag. Mat. 215-216 (2000) 264-267.

[19]   H.E. Kissinger, J. Res. Nat. Bur. Stand. 57 (1956) 217-221.

[20]   Wijn HPJ. Landolt-Börnstein: Magnetische Eigenschaften von Metallen, vol. 19. Berlin: Springer; 1991. pp. 92-94.

[21]   R. Ray, R. Hasegawa, Solid State Comm. 27 (1978) 471-474.

[22]   J.J. Ipus, J.S. Blázquez, V. Franco, M. Stoica, A. Conde, J. Appl. Phys. (2014) in press.

[23]   A. Blachowski, K. Ruebenbeuer, J. Zukrowski, Phys. Stat. Sol. B 242 (2005) 3201-3208.

[24]   M. Kobayashi, T. Kai, N. Takano, Y. Ohashi, K. Shiiki, J. Mag. Mag. Mat. 166 (1997) 329-333.

[25]   C.F. Conde, M. Millán, A. Conde, J. Mag. Mag. Mater 138 (1994) 314-318.

Table caption

Table 1. EDX data for powder samples milled 40 h.

Table 2. Peak temperature, T_p, and activation energy, E_A, of the crystallization process for B-containing alloys after 40 h milling.

Table 1. EDX data for powder samples milled 40 h.

Alloy	Fe/(Fe+Nb)		Cr [at.%]
	Nominal	EDX	
c-B	0.882	0.885	0.52
a-B	0.882	0.885	0.96
a2-B	0.884	0.886	0.98
FeB	0.882	0.889	0.75

Table 2. Peak temperature, T_p, and activation energy, E_A, of the crystallization process for B-containing alloys after 40 h milling.

Sample	T_p [K] (±1)	E_A [eV] (±0.2)
c-B	855	5.7
a-B	848	4.9
a2-B	846	4.8
FeB	872	4.6
Ribbon	852	4.4

Figure captions

Figure 1. XRD patterns of the initial boron powder used to prepare the different samples: (a) commercial crystalline B, (b) commercial amorphous B and powders milled up to 50 h (arrow indicates increasing of milling time) and (c) intermetallic FeB. (d) SEM image in BSE mode for raw FeB powder.

Figure 2. XRD patterns for studied alloys after: (a) 0.5h, (b) 4 h and (c) 40 h milling.

Figure 3. Milling time evolution of fraction of bcc-Nb phase.

Figure 4. Crystalline fraction as a function of milling time.

Figure 5. Mössbauer spectra for the studied alloys after 40 h milling.

Figure 6. Fraction of Fe atoms with $HF \leq 5T$ contribution as a function of milling time.

Figure 7. SEM BS images for (a) c-B, (b) a-B, (c) a2-b and (d) FeB sample after 40 h milling. TEM HAADF images for (e) c-B (taken from [11]), (f) a-B, (g) a2-B and (h) FeB alloy after 40 h milling.

Figure 8. Bright field image of a2-B sample after 40 h milling. Insets correspond to SAED pattern and EELS spectra taken on the corresponding points.

Figure 9. DSC scans at 40 K/min for all studied samples after 40 h milling. DSC scan of as-spun ribbon is shown for comparison.

Figure 10. Spontaneous specific magnetization as a function of milling time.

Figure 11. Curie temperature of amorphous phase as a function of milling time for B-containing alloys.

Figure 12. Milling time dependence of (a) lattice parameter, (b) crystal size and (c) microstrains for the crystalline contribution.

Figure 13. Nb concentration as a function of milling time, estimated from Mössbauer results.

Figure 14. Specific magnetization as a function of Nb content for theoretical data of binary $Fe_{100-X}Nb_X$ system [24] along with experimental data for n-B alloy.

Figure 15. B dependence of the Curie temperature of amorphous $Fe_{100-Y}B_Y$ system [20] and predicted behavior for $Fe_{90-Z}Nb_{10}B_Z$ system along with the experimental T_C data after 40 h milling.

Figure 16. Estimation of dissolved boron in the amorphous matrix for all the B-containing samples after milling time above 10 h.

Figure 1
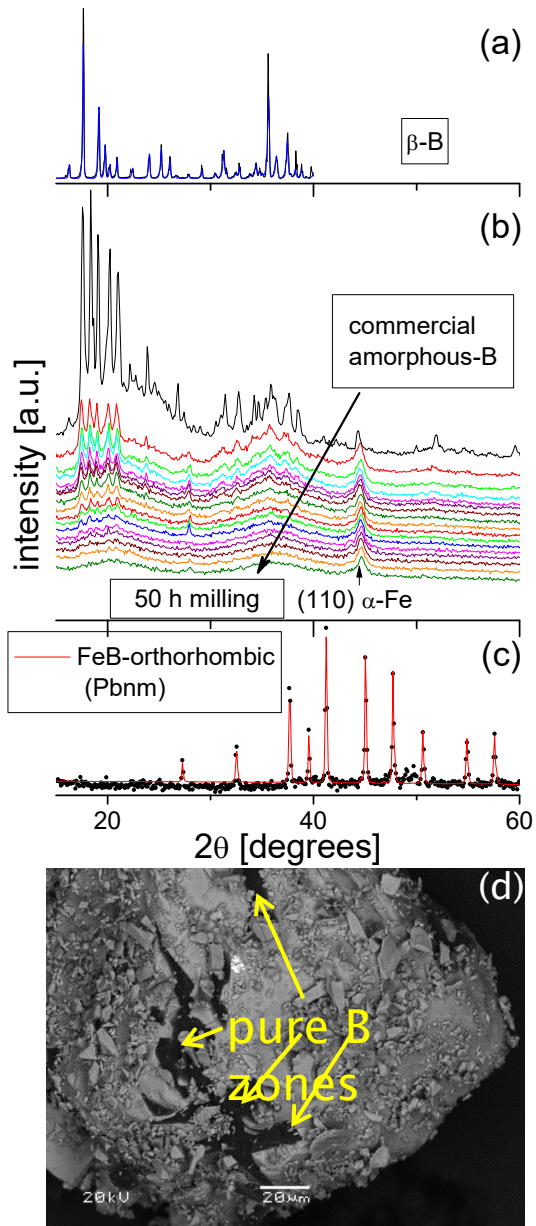
Figure 2
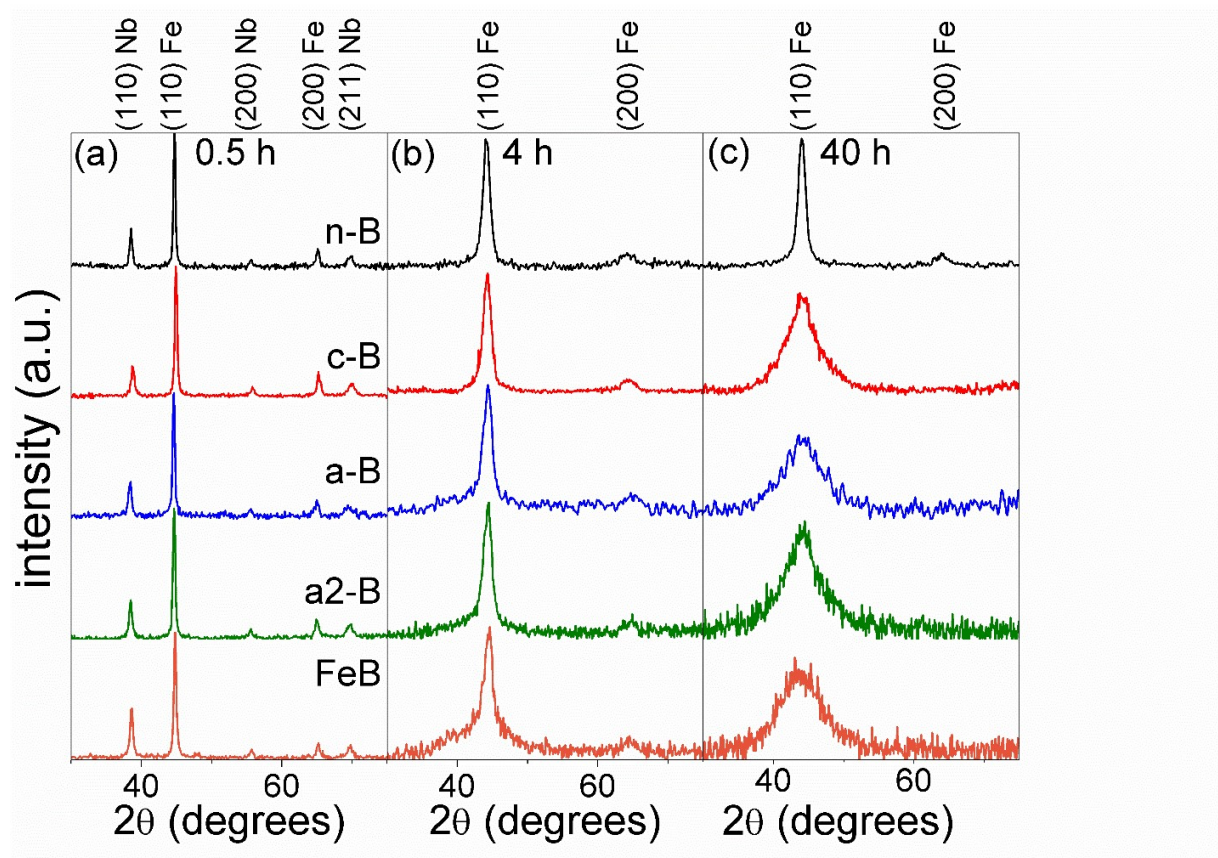
Figure 3
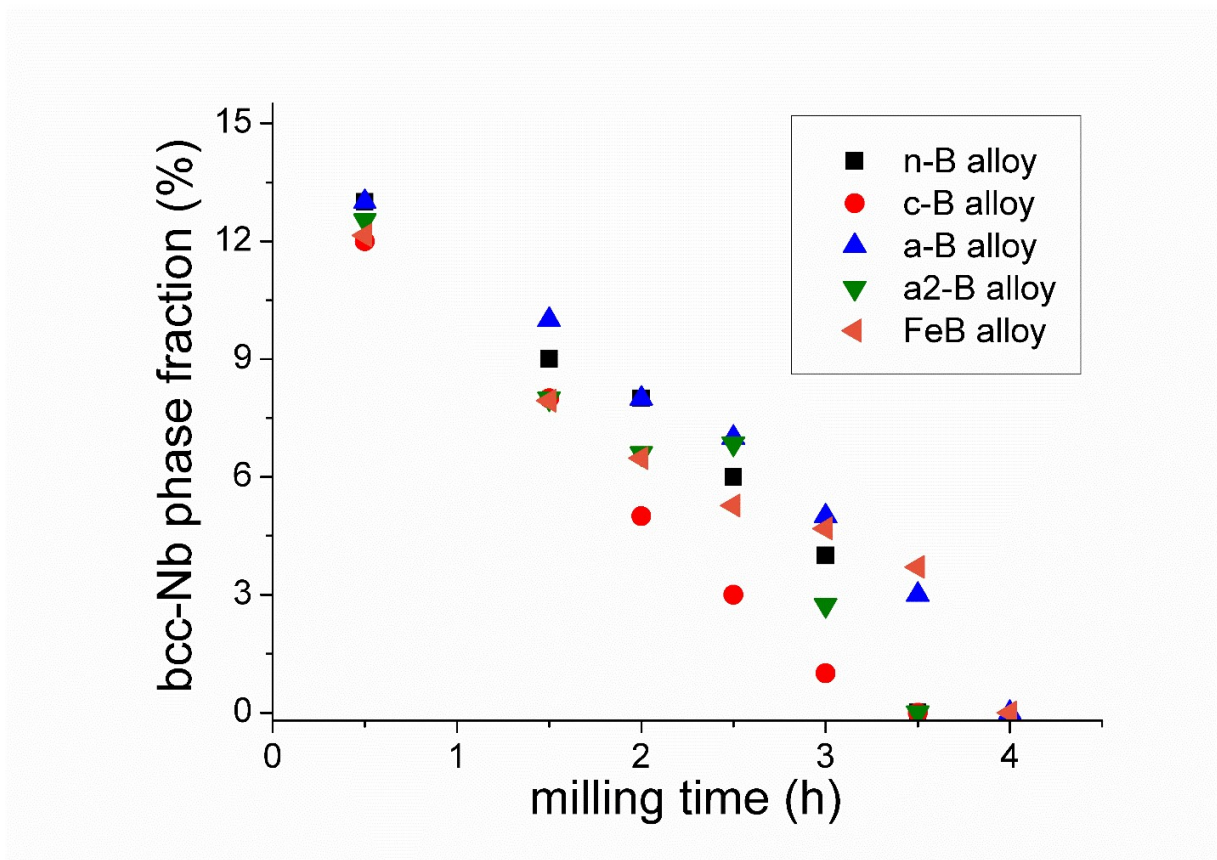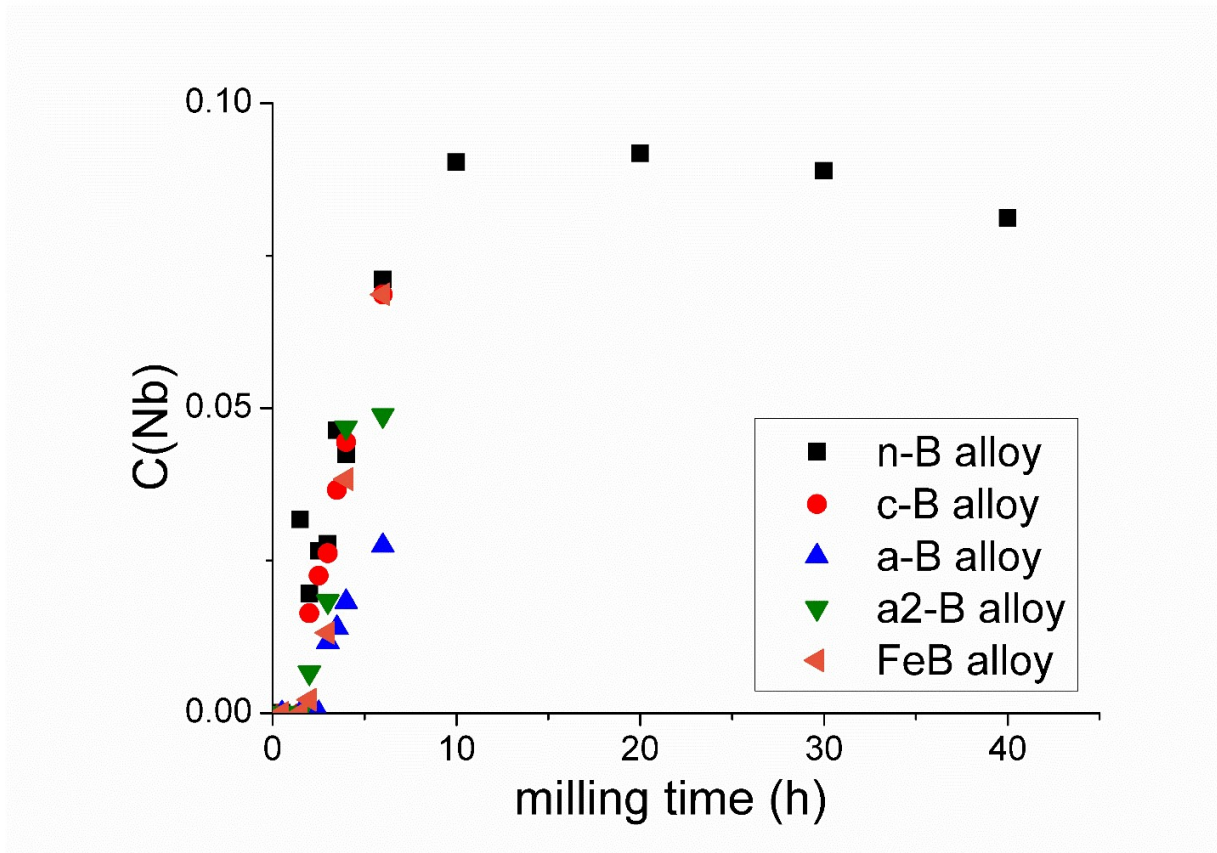
Figure 4
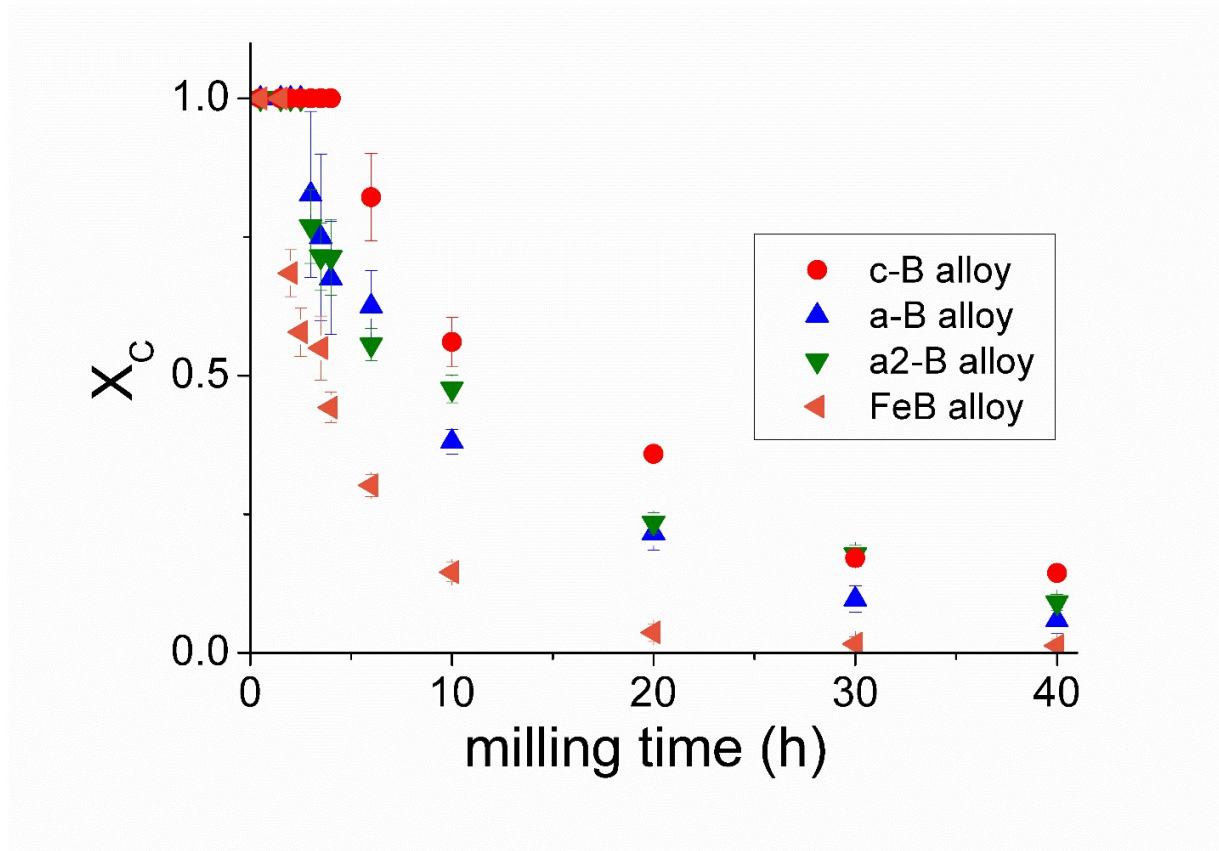
Figure 5
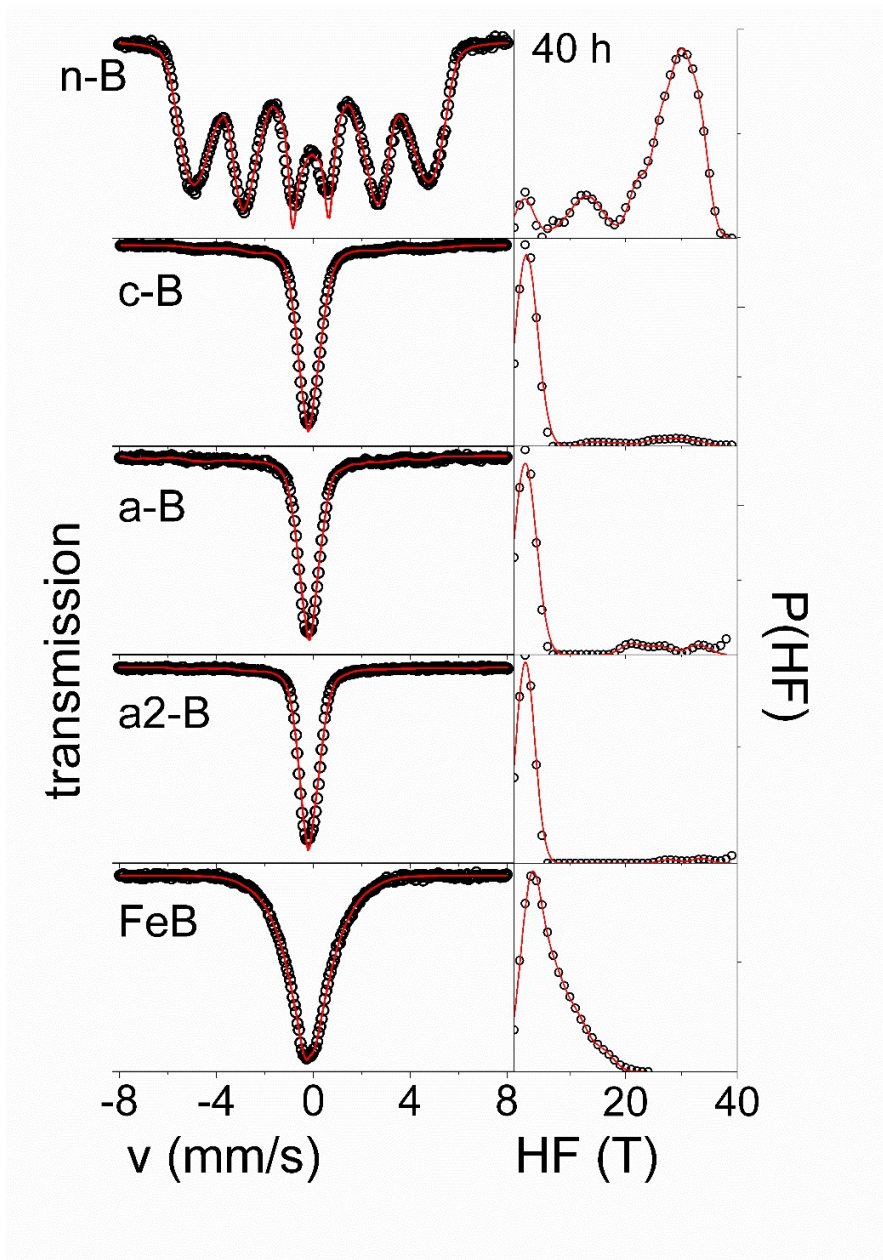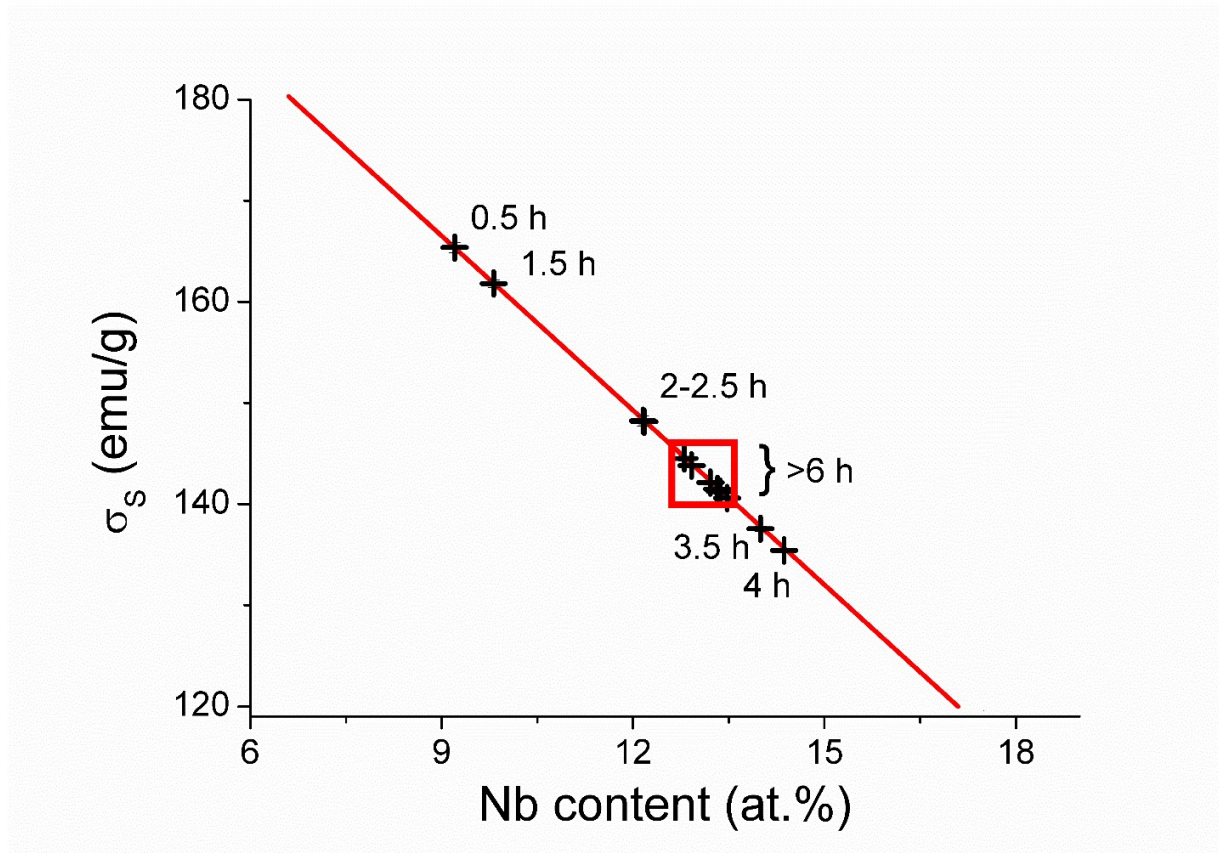
Figure 6
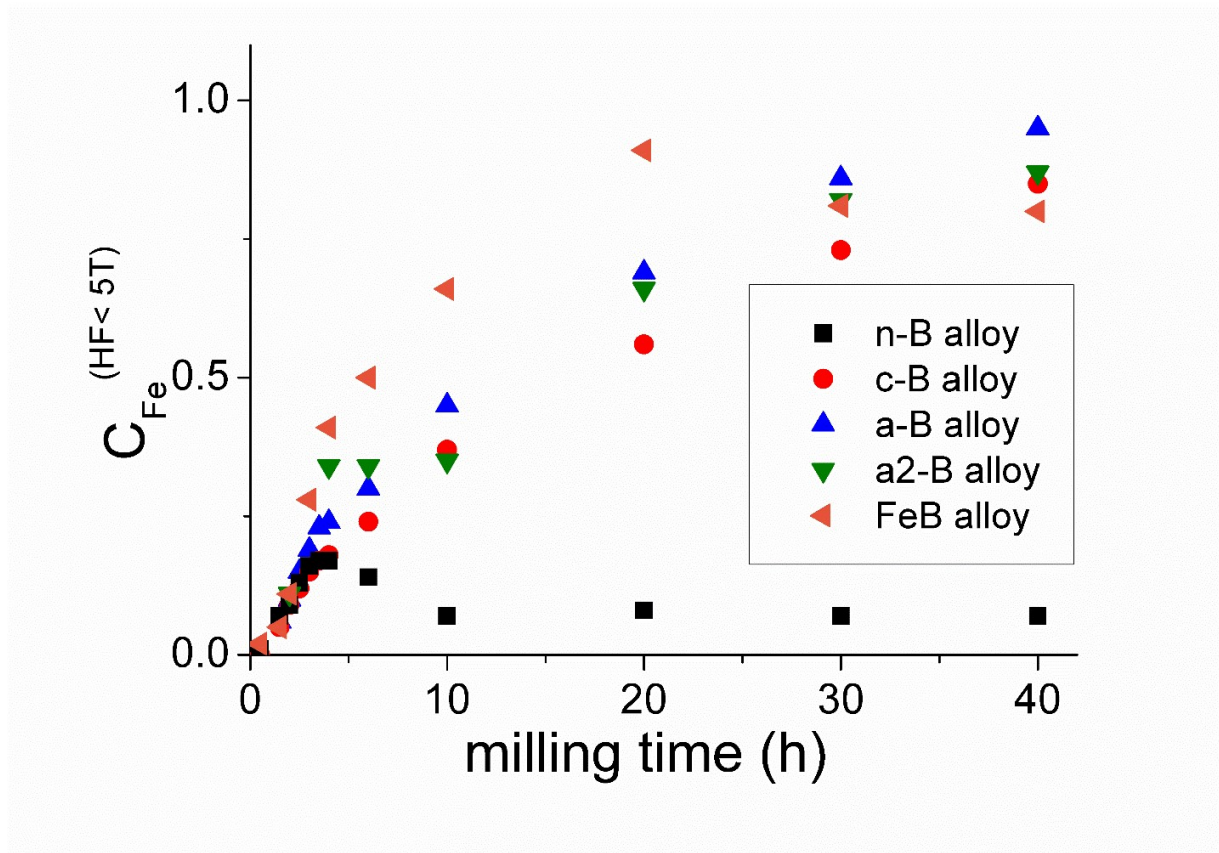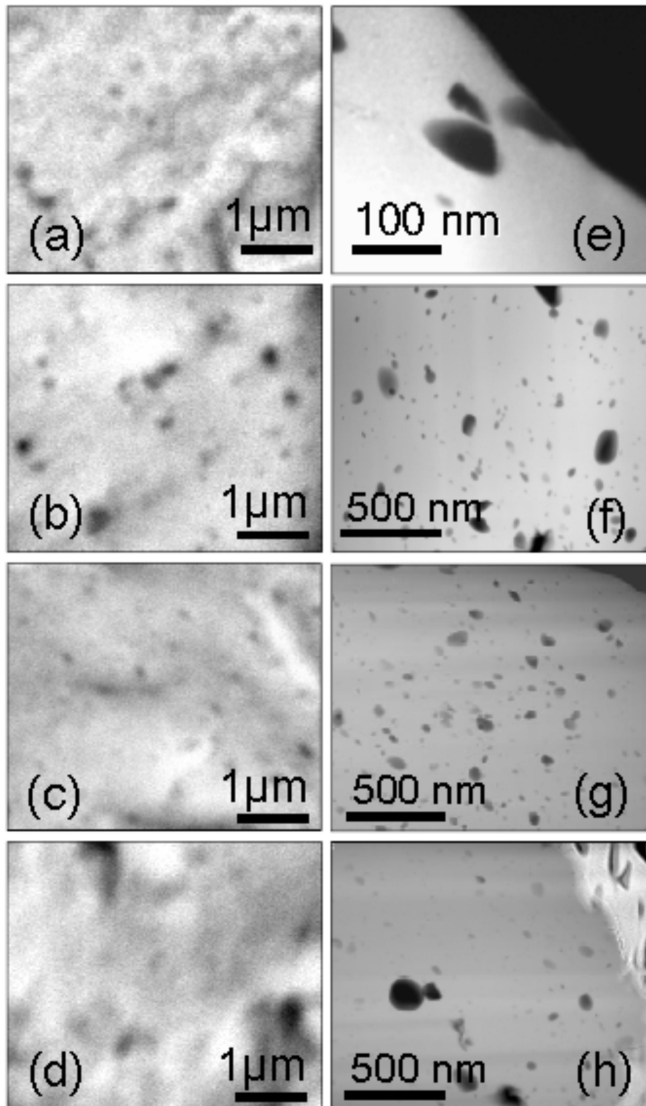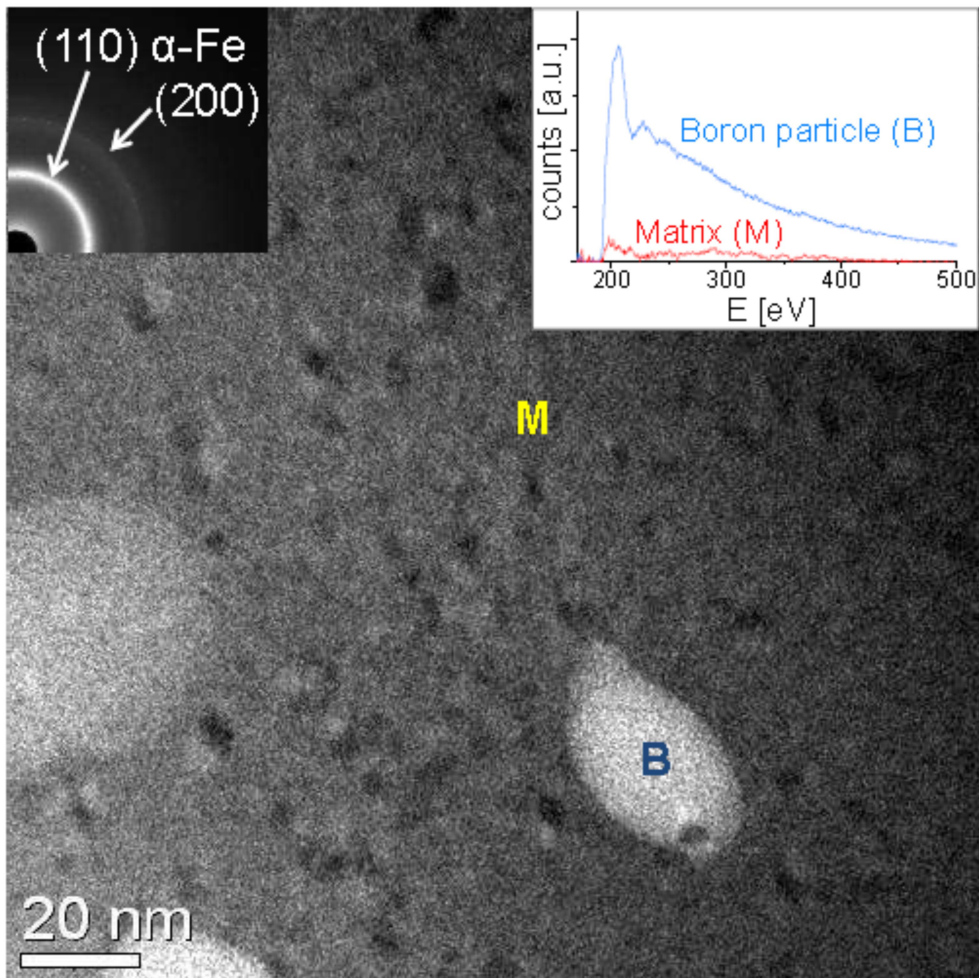
Figure 7
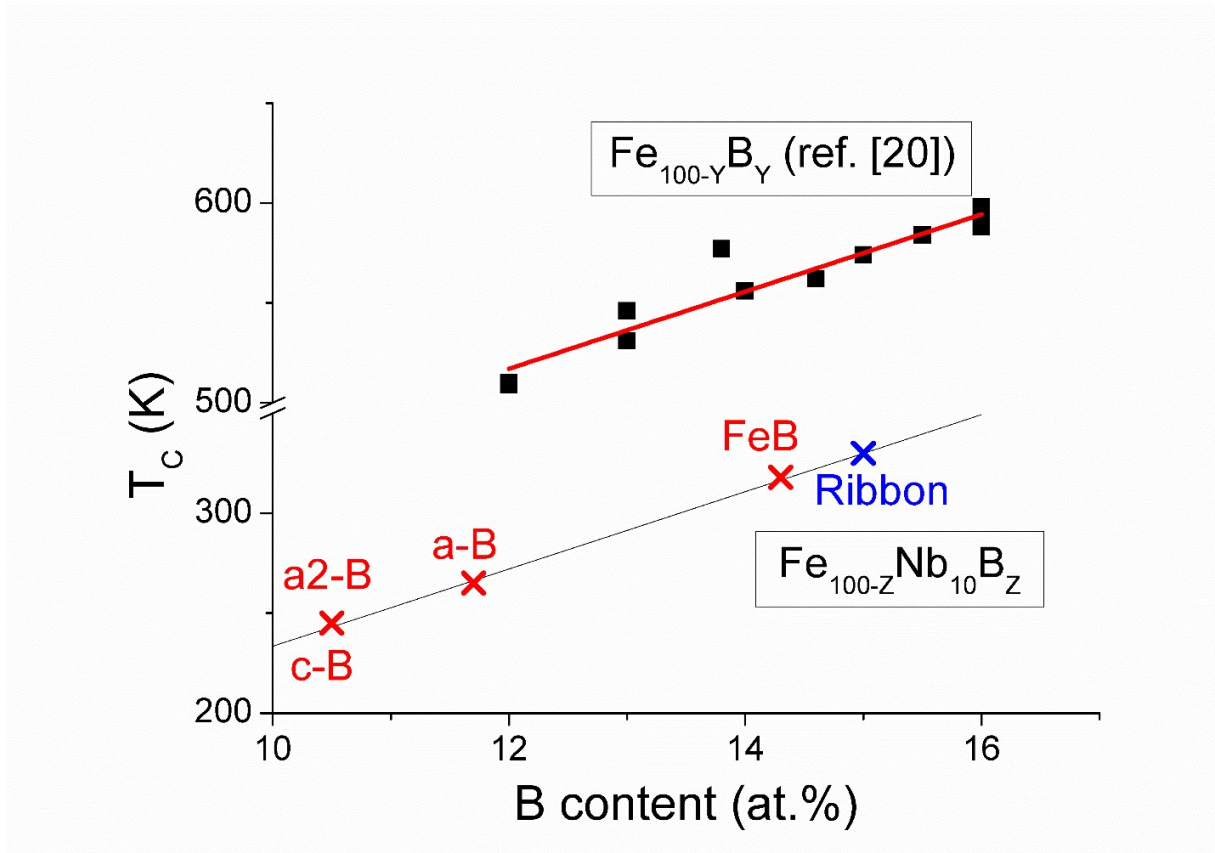
Figure 8

Figure 9
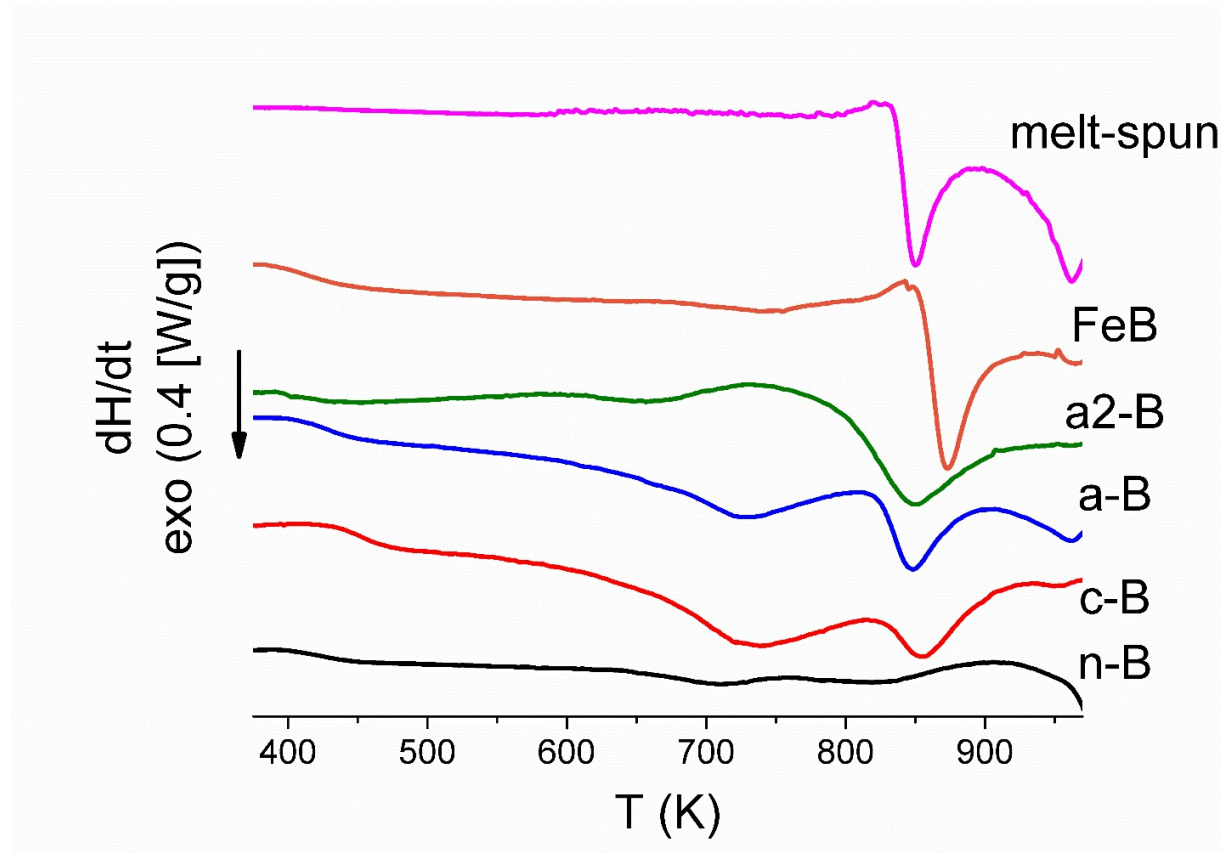
Figure 10
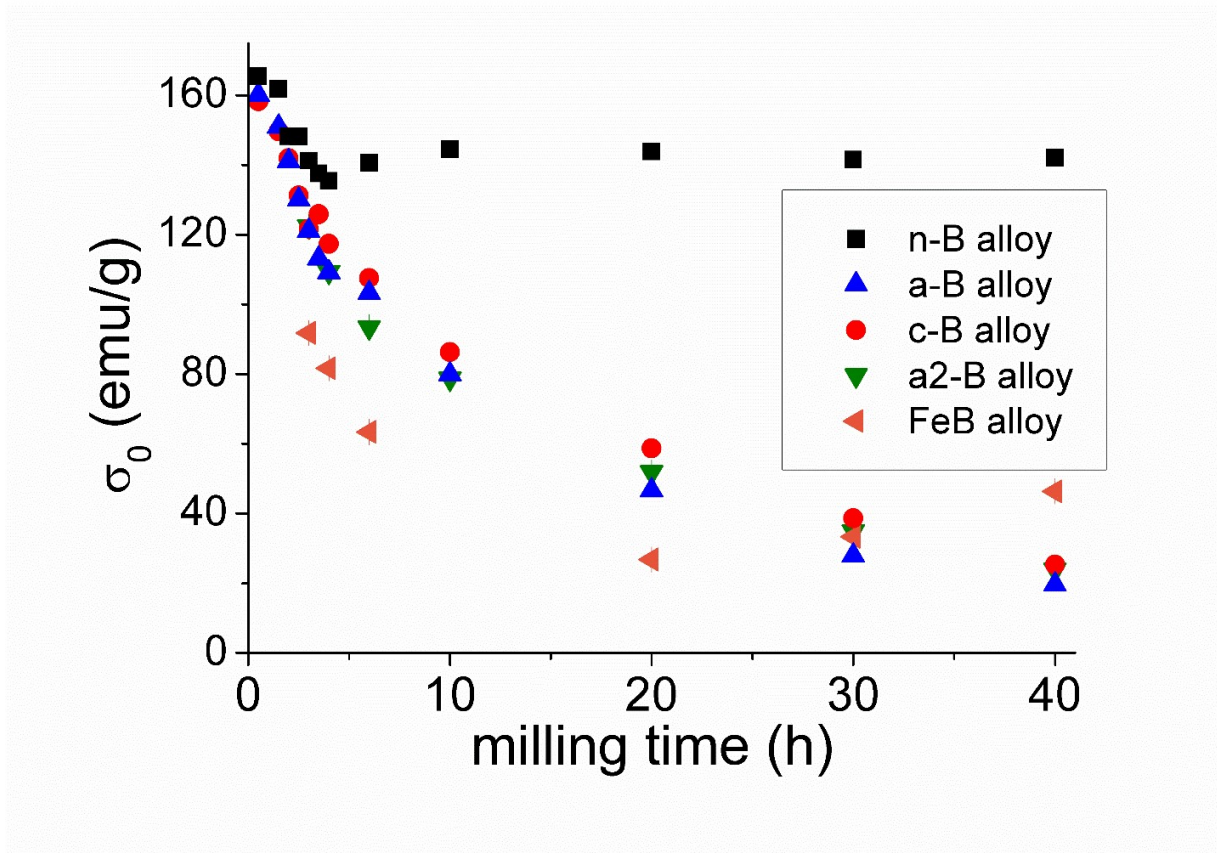
Figure 11
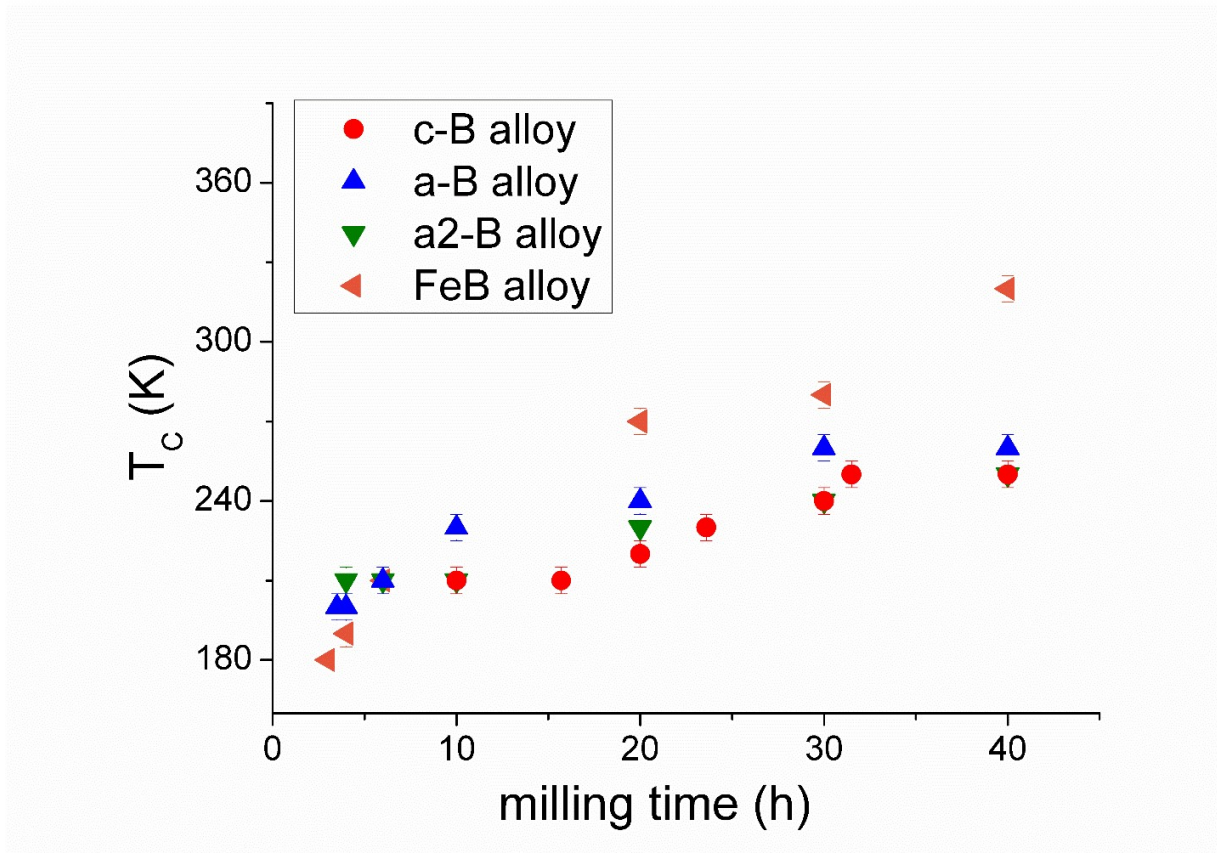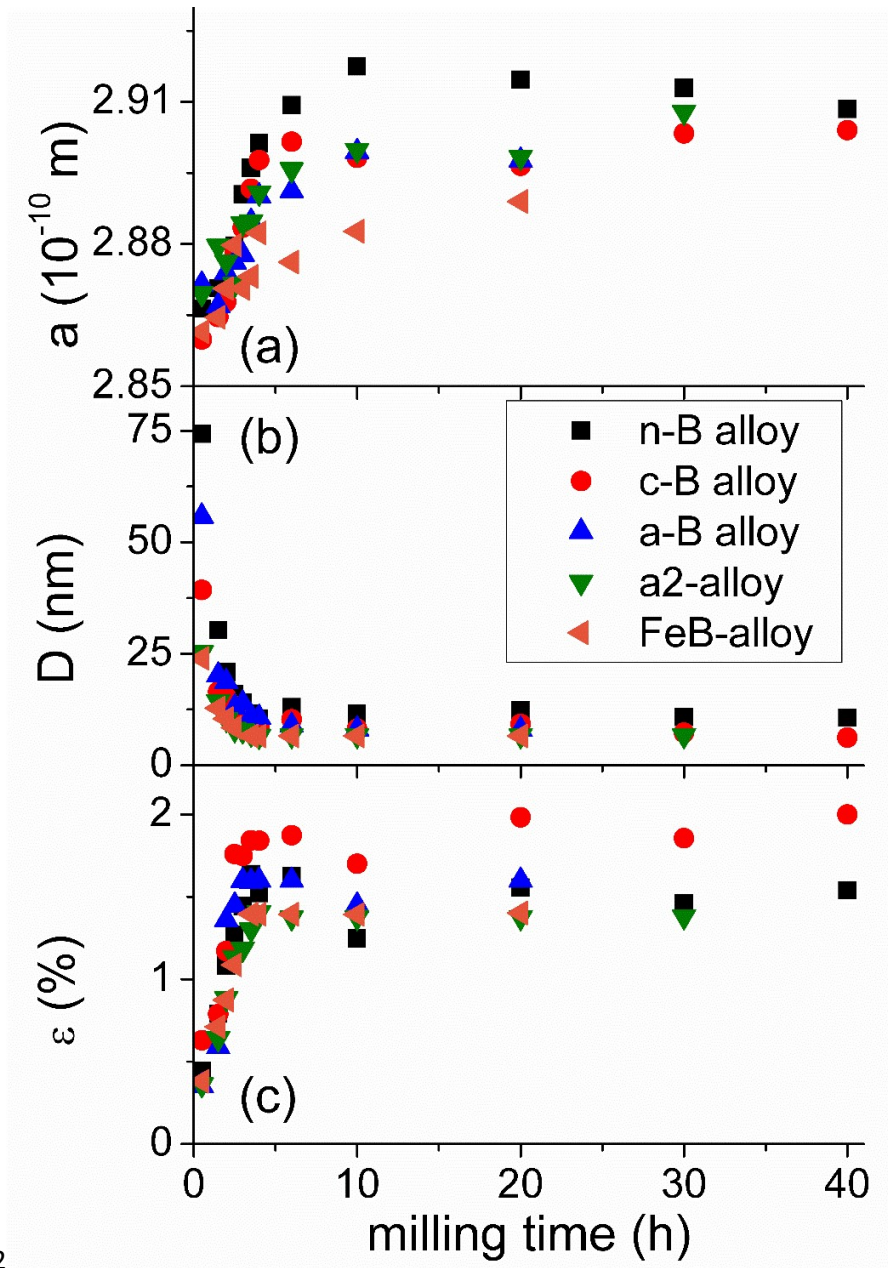
Figure 12

Figure 13

Figure 14

Figure 15

Figure 16